van den Heuvel, D. B., Gunnlaugsson, E., Benning, L. G. (2020): Surface roughness affects early stages of silica scale formation more strongly than chemical and structural properties of the substrate. - Geothermics, 87, 101835.

https://doi.org/10.1016/j.geothermics.2020.101835

Surface roughness affects early stages of silica scale formation more strongly than chemical and structural properties of the substrate

Daniela B. van den Heuvel[a]*, Einar Gunnlaugsson[b], Liane G. Benning[a,c,d]

[a]Cohen Geochemistry Group, School of Earth and Environment, University of Leeds, Leeds LS2 9JT, United Kingdom

[b]Reykjavik Energy, Baejarhals 1, 110 Reykjavik, Iceland

[c]German Research Center for Geosciences, GFZ, 14473, Potsdam, Germany

[d]Department of Earth Sciences, Free University of Berlin, 12249 Berlin, German

[*]corresponding author: daniela.vandenheuvel@geo.unibe.ch; current address: Rock-Water Interaction Group, Institute of Geological Sciences, University of Bern, 3012 Bern, Switzerland

Keywords: Silica, geothermal energy, precipitation, scaling, heterogeneous nucleation

Abstract

Precipitation of amorphous silica (SiO_2) in geothermal power plants has been shown to occur via homogeneous nucleation in the separated water as well as heterogeneous nucleation on pre-existing surfaces. While the factors facilitating homogeneous nucleation are well known, the effect of surface properties on the heterogeneous pathway are less well understood. We investigated the precipitation of amorphous silica onto different surfaces by placing coupons of opal (= mirroring previously deposited silica), volcanic glass (= common reservoir rocks) and corrosion-resistant carbon steel (= geothermal pipelines) inside the pipelines of the Hellisheiði power plant (SW-Iceland) where they were in contact with a silica-supersaturated

geothermal liquid (800 ppm SiO_2, 60 to 120 °C) for up to 10 weeks. Our results showed that the similarities in chemical composition and structure of opal and volcanic glass to the amorphous silica were less important in facilitating nucleation than the rough surface of the carbon steel. However, once the nuclei had formed, their growth was independent of the surface material and only controlled by deployment length, temperature and the concentration of monomeric silica in the separated water. Thus, over time a continuous, botryoidal silica layer formed on all coupons. This suggests that surface properties are not crucial in developing better mitigation strategies against amorphous silica scaling.

1. Introduction

Silica (SiO_2) is the most common chemical compound in the Earth's crust and dissolved silica a major component in most high-enthalpy geothermal fluids. When such fluids are flashed and cooled during power generation, they become supersaturated with respect to amorphous silica, which leads to rapid precipitation. This unwanted precipitation (scaling) inside pipelines and onto other fluid-handling equipment is a major issue in geothermal power plants around the world, decreasing the efficiency of geothermal energy production (Gudmundsson and Bott, 1979; Rothbaum et al., 1979; Harrar et al., 1982; Yokoyama et al., 1993; Gunnarsson and Arnórsson, 2005; Padilla et al., 2005; Meier et al., 2014; Dixit et al., 2016; Mroczek et al., 2017).

Amorphous silica scales exhibit two different morphologies: (1) "fluffy" and soft silica precipitates consisting of individually deposited and (partly) cemented colloids and (2) dense, hard silica layers, often with a botryoidal surface and no internal structure (Thórhallsson et al., 1975; Gudmundsson and Bott, 1979; Rothbaum et al., 1979; Brown and McDowell, 1983; Carroll et al., 1998). Our recent study (van den Heuvel et al., 2018) of

49 silica scales inside the pipelines of the Hellisheiði power plant (SW-Iceland) found that these
50 two morphologies can be attributed to two different silica precipitation pathways: The
51 homogeneous pathway starts with homogeneous nucleation of nanoparticles in the liquid,
52 which then grow by addition of dissolved silica or are aggregated to µm-sized spheres.
53 Subsequently these particles are deposited onto available surfaces where they can form
54 complex 3D structures. For the heterogeneous pathway, silica precipitates by heterogeneous
55 nucleation directly onto available surfaces. The nuclei subsequently grow to individual half-
56 spheres by addition of dissolved silica from the liquid. Over time, this leads to the formation
57 of a botryoidal silica layer.

58 From a plethora of laboratory studies we know that favourable physicochemical
59 conditions such as high total silica concentrations, high percentage of monomers, elevated
60 temperature and high pH enhance silica polymerisation and thus silica scaling (Alexander et
61 al., 1954; Goto, 1956; Kitahara, 1960; Iler, 1979; Crerar et al., 1981; Weres et al., 1981;
62 Fleming and Crerar, 1982; Gallup, 1997; Gunnarsson and Arnórsson, 2005; Icopini et al.,
63 2005; Tobler et al., 2009; Tobler and Benning, 2013). This in turn favours both types of
64 nucleation as well as growth of silica particles and half-spheres. Besides the physicochemical
65 conditions of the liquid, the heterogeneous pathway also depends on surface properties such
66 as surface roughness and composition and structure of the substrate. Rough surfaces enhance
67 heterogeneous nucleation as they reduce the contact angle of the nuclei with the surface
68 which in turn reduces the interfacial energy and the energetic barrier for nucleation to occur
69 (De Yoreo and Vekilov, 2003; Benning and Waychunas, 2007). This has been shown
70 experimentally and by numerical simulations for a range of different materials onto different
71 substrates (e.g. Qi et al., 2004; Järn et al., 2006; Page and Sear, 2009; Campbell et al., 2013).
72 The effect of surface chemistry on heterogeneous nucleation has been evaluated by
73 investigating mineral precipitation onto different mineral substrates. One factor enhancing

mineral precipitation is the presence of ions in the mineral substrate which are needed for the nucleation of the secondary phase (Putnis, 2009 and references therein). Another aspect enhancing mineral nucleation is a lattice match between the substrate and the secondary phase, i.e. surfaces with a similar structure can act as a template for the nucleation of new materials. (e.g. De Yoreo and Vekilov, 2003; Fernandez-Martinez et al., 2012; Murray et al., 2012; Stockmann et al., 2014; Zolles et al., 2015). Based on all these studies, we would expect that rough and/or silica(te)-based surfaces (e.g. the reservoir rocks) are more prone to silica deposition than smooth and/or non-silica(te) surfaces (e.g. the inside of geothermal pipelines). In order to test this hypothesis, we investigated three surfaces with different chemical compositions and roughness: non-precious opal, volcanic glass and carbon steel. In addition, we compared the results presented here to our previous study investigating silica scaling inside the pipelines of the Hellisheiði power plant onto stainless steel (van den Heuvel et al., 2018) as the scaling plates for both studies were deployed at the same time and the silica thus precipitated under identical physicochemical conditions.

2. Materials and methods

Three different substrates (non-precious opal, volcanic glass and S275 carbon steel) were chosen to investigate the effect of surface properties on silica deposition. Coupons (2 x 1.3 cm) were prepared from each material and then glued onto S316 stainless steel plates (5.4 x 2 cm) using a Loctite Hysol 9455 epoxy adhesive. Equivalent coupons of each material were imaged pre-deployment using a field emission gun scanning electron microscope (FEG-SEM, FEI Quanta 650 at 15 keV). In addition, chemical analyses of the major and trace elements of the volcanic glass and the opal were performed on pressed powder tablets (32 mm diameter, 4g sample + 0.9g Höchstwax as binder) using a Philipps WD-XRF PW2400 and the UniQuant 5 software (Omaga Data Systems) at the University of Fribourg.

The composition of the S275 carbon steel was provided by the manufacturer (RS Components Ltd UK). Once prepared, the scaling plates were shipped to the Hellisheiði geothermal power plant ~30 km SE of Reykjavik, Iceland. Geothermal power plants are well-suited sites for the study of silica precipitation as the conditions at each location within the pipelines are relatively constant (small variation in temperature, flow rate and fluid chemistry; Table 1) and well constrained due to constant monitoring. Two deployment locations were chosen for this study (Figure 1A): Location A was located <10 m upstream from the heat exchanger, while Location B was located several tens of metres after the heat exchanger. The two locations differ with respect to temperature as the separated water is cooled from 120 °C to 60 °C inside the heat exchanger. In addition, Location B shows a lower flow rate due to changes in pipe geometry. Both locations were downstream from the steam separators, where the steam used for the powering of the turbines is separated, silica supersaturation is reached and precipitation starts to occur. For each deployment, a simple stainless steel scaling plate and a stainless steel plate with glued on coupons were attached to a sampling rod and inserted into the pipelines through valves (Figure 1B - D). The silica precipitates which formed on the glued-on coupons will be described here while the silica deposited onto the pure stainless steel scaling plates were described in van den Heuvel et al., 2018.

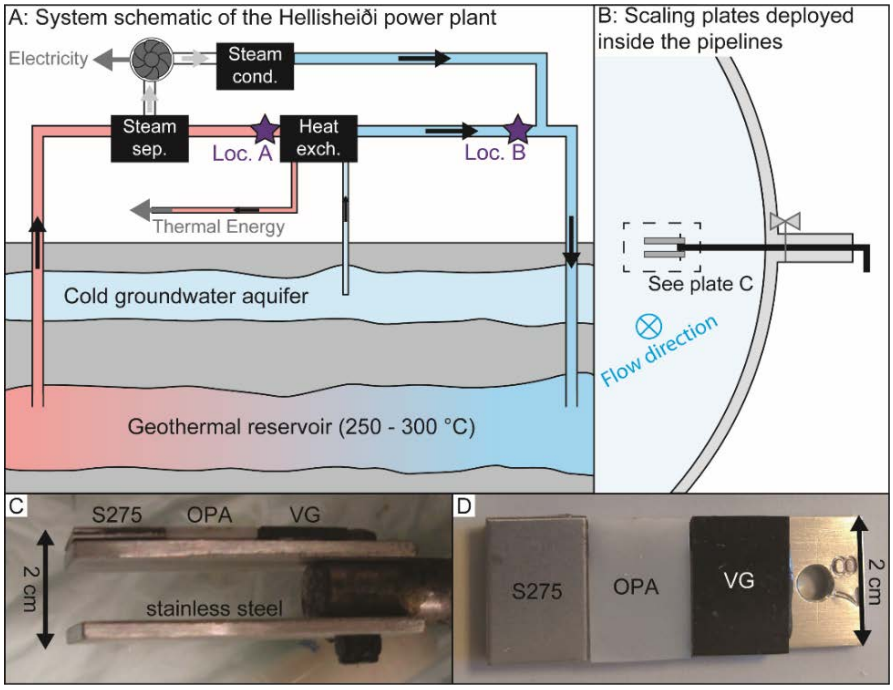

Figure 1: Simplified system schematic of the Hellisheiði power plant (steam sep. = steam separator, steam cond. = steam condenser, heat exch. = heat exchanger) showing the two sampling locations (A), the deployment set-up (B & C) and photographs of the scaling plates before deployment (C & D). VG = volcanic glass, OPA = non-precious opal and S275 = carbon steel).

To monitor silica precipitation as a function of time, scaling plates were left to react with the separated water inside the pipelines for 1 day, 1 week, 2 weeks, 4 weeks, 6 weeks and 10 weeks. At the beginning and end of each deployment, the separated water was sampled by filtration through 0.2 µm polycarbonate filters and aliquots of the filtered liquid were preserved for analysis of anions, cations, total dissolved silica, molybdate-reactive silica, total carbonate carbon (TCC) and total sulphide sulphur (TSS). The amount of particulate silica was determined by passing 2 L of separated water through pre-weighted 0.2 µm polycarbonate membranes. All membranes were dried at 40 °C for ~16 h and subsequently re-weighed, the weight difference corresponding to the particle load in the

separated water. FEG-SEM imaging (specifications see above) and energy-dispersive X-ray spectroscopy (EDS spot analyses, AZtec soft-ware, Oxford Instruments, Version 2.2) confirmed that silica spheres were by far the dominant component in the filter residue. "Polymeric" silica (any molybdate-unreactive silica that passes through the < 0.2 μm filter membranes) was determined by subtracting the concentration of molybdate-reactive silica from the total silica concentration. For more details of the liquid sampling and subsequent analyses, see van den Heuvel et al. (2018). The temperatures and flow rates inside the pipelines were recorded hourly by the power plant operators at both locations.

Table 1: Compositions of the three types of coupons used in this study.

	Opal (OPA)[1]		Volcanic glass (VG)[1]		Carbon steel (S275)[2]	
Composition [wt.%]	SiO_2	92.5	SiO_2	69.5	Fe	> 98.0
	Al_2O_3	2.1	Al_2O_3	13.7	Mn	< 1.6
	Na_2O	0.3	Na_2O	4.8	C	< 0.25
	CaO	0.5	CaO	1.5	Si	< 0.05
	K_2O	0.2	K_2O	3.5	S	< 0.05
	MgO	0.1	MgO	0.2	P	< 0.04
	Fe_2O_3 (tot.)	0.2	Fe_2O_3 (tot.)	5.1		
	LOI	3.7	LOI	0.1		

[1]Composition derived from the XRF analyses with LOI (loss ion ignition) at 1050 °C

[2]Composition as provided by the manufacturer (RS Components Ltd UK)

The saturation indices of amorphous silica under in-situ conditions were determined using PHREEQC (version 3.0, Parkhurst and Appelo, 2013) with the phreeqc.dat database, supplemented with solubility data for amorphous silica from Gunnarsson and Arnórsson

(2000). The temperature values and composition of the separated water listed in Table 2 were used as input data. At the end of each deployment, the plates were removed from the liquid, gently rinsed with distilled water to prevent the precipitation of salts and/additional silica and then dried at 30°C for 24 h. Subsequently, they were photographed and, where possible, precipitates from one half of each coupon were scraped off with a plastic spatula. These precipitates were ground using an agate mortar and pestle and the powders analysed by X-ray diffraction (XRD, Bruker D8, CuKα1; 5-90° 2θ, 0.01°/step). All scaling plates were then coated with ~40 nm of gold, imaged using FEG-SEM and analysed by energy-dispersive X-ray spectroscopy (specifications see above). Based on the FEG-SEM images, the dimensions of the observed structures were determined by manually measuring widths and lengths of 70 to 100 silica half spheres which make up the botryoidal layer on each coupon.

3. Results

3.1 Characterisation of the separated water

The liquid at Locations A and B was identical with respect to composition (Table 2). The differences between the two locations were temperature and flow rate, which were both higher at Location A (~ 120°C vs. ~60 °C and ~420 L/s vs. 280 L/s, respectively). The 800 ppm of silica measured are present as dissolved silica. At Location A, 85% of this silica occurs as molybdate-reactive silica (primarily H_4SiO_4 but including an unknown proportion of silica dimers and trimers) while at Location B this value is lower (76 %). In addition silica particles with highly variable diameters (<0.1 to 22.7 μm) and a mean particle size of 0.2 μm at Location A and 0.1 μm at Location B were suspended in the separated water. They make up less than 0.03 wt.% of total silica. At both locations, the separated water is slightly supersaturated with respect to amorphous silica (Table 2).

Table 2: Average and standard deviation of temperature, flow rate and composition of the separated water for Locations A and B (from van den Heuvel et al., 2018).

		Loc. A[1]	Loc. B[1]
Temp.	[°C]	117.8 ± 0.4	58.0 ± 5.3
Flow rate	[l/s]	416 ± 54	282 ± 18
SiO_2	[ppm]	802 ± 19	794 ± 30
monom.[2]	[%]	85	76
polym.[2]	[%]	15	24
Na	[ppm]	204 ± 8	207 ± 8
Cl	[ppm]	173 ± 12	175 ± 6
K	[ppm]	34.7 ± 1.6	35.1 ± 1.6
TCC[3]	[ppm]	25.4 ± 5.5	23.8 ± 3.7
TSS[4]	[ppm]	19.2 ± 2.9	20.5 ± 1.9
Al	[ppm]	1.99 ± 0.09	2.04 ± 0.11
Ca	[ppm]	0.71 ± 0.13	0.71 ± 0.04
Fe	[ppb]	7.6-27.8	5.7-58.9
Mg	[ppb]	3.2-70.1	<1.1-42.2
pH meas.[5]	[-]	9.4 ± 0.2	9.4 ± 0.2
pH calc.[6]	[-]	8.5 ± 0.1	9.0 ± 0.1
Eh[6]	[V]	-0.56 ± 0.01	-0.47 ± 0.01
SI SiO_2 (am)[7]	[-]	0.10 ± 0.02	0.42 ± 0.02

[1]Correspond to Locations 1 and 3 in Meier et al. (2014) and van den Heuvel et al. (2018).

[2]Molybdate-reactive silica determined based on the method by Gunnarsson et al. (2010). Polymeric silica determined by subtracting the molybdate-reactive silica from total silica. Represent maximum (molybdate-reactive silica) and minimum (polymeric silica) values, respectively, as some depolymerisation of polymeric silica due to dilution during sampling cannot be excluded.

[3]Total carbonate carbon determined by alkalinity titration as described by Arnórsson et al. (2006).

[4]Total sulfide sulphur determined by titration as described by Arnórsson et al. (2006).

[5]As measured on-site after cooling the separated water to 21 – 27 °C.

[6]Derived from PHREEQC simulations at measured in-situ temperatures and with the analysed fluid compositions.

[7]Calculated using PHREEQC (version 3.0, Parkhurst and Appelo, 2013) with the phreeqc.dat database, updated with the thermodynamic data for amorphous silica from Gunnarsson and Arnórsson (2000).

188 3.2 Description of coupon materials pre-deployment

189 The opal was chosen as a coupon material due to its structural and chemical similarity to
190 silica scales. Both are composed of randomly stacked and partially cemented silica
191 microspheres (Wollaert et al., 1990; van den Heuvel et al., 2018). The surface of the opal
192 coupons was polished and when imaged by FEG-SEM, appeared completely smooth (Figure
193 2A), except for a couple of small (< 2 mm) superficial scratches. In addition, some damage
194 was observed along the edges of the coupons, where small pieces (mm-sized) of opal had
195 chipped off (Figure 2E). This damage occurred during the transport to Hellisheiði or while
196 mounting the samples onto the sample holder pre-deployment. Damage post-deployment can
197 be excluded as the fracture edges formed enhanced silica particle deposition from the liquid
198 (see below).

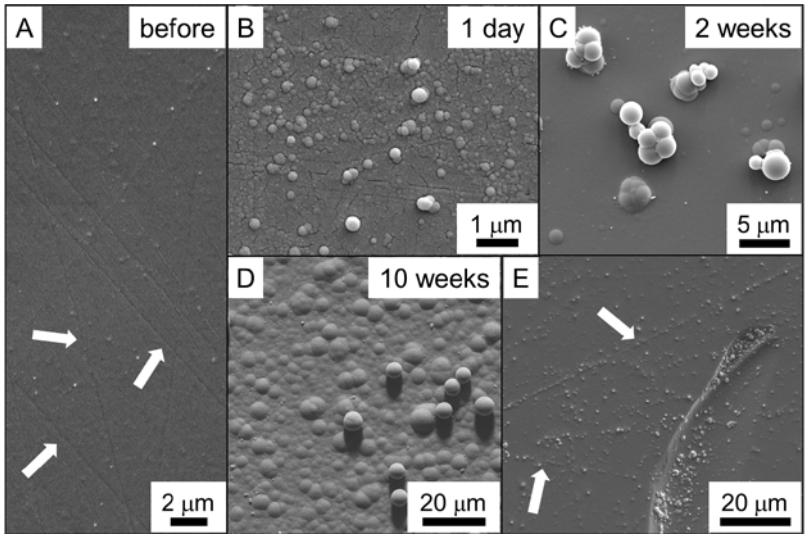

199

200 *Figure 2: FEG-SEM microphotographs of the opal (OPA) surface (A) before deployment*
201 *(scratches on the surface highlighted with arrows in the bottom half of the photograph), (B)*
202 *after 1 day, (C) after 2 weeks, (D) after 10 weeks and (E) two scratches (highlighted with*
203 *arrows) acting as preferential nucleation sites as well as a conchoidal fracture enhancing the*
204 *deposition of silica microspheres (1 day deployment). All microphotographs are from*
205 *samples deployed at Location B.*

206 The volcanic glass was chosen as a substrate due to its structural and chemical
207 similarity with the basaltic hyaloclastites of the Hellisheiði geothermal field (Alfredsson et
208 al., 2013). While not an exact chemical match (the glass chosen here was more acidic with
209 nearly 70 wt.% SiO_2), the surface properties and the solubility of different alumosilicate
210 glasses have been shown to be comparable, with lower dissolution rates for more acidic
211 glasses (Wolff-Boenisch et al., 2004). Prior to deployment, the polished volcanic glass
212 coupons were characterised by smooth surfaces with few scratches and numerous tube-like or
213 spherical vesicles ranging from a few micrometres to 2 mm in size (Figure 3A).

214

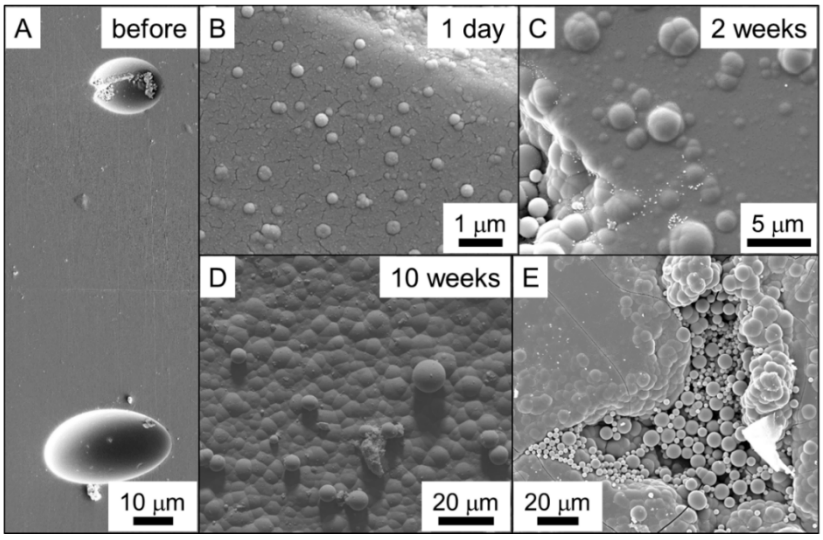

215

216 *Figure 3: FEG-SEM microphotographs of the volcanic glass (VG) surface (A) before*
217 *deployment, (B) after 1 day, (C) after 2 weeks, (D) after 10 weeks and (E) a close-up of a*
218 *vesicle filled by silica microspheres (4 week deployment). All microphotographs are from*
219 *samples deployed at Location B, except plate (E) which shows a sample deployed at Location*
220 *A.*

221

222 The tinned S275 carbon steel was used as a readily available, relatively corrosion
223 resistant analogue for the high-grade carbon steel (P235GH, EN 10028-2-2003) from which

224 the pipelines at Hellisheiði are fabricated. The main difference between the two steels is the
225 presence of up to 0.3 % chromium in P235GH, resulting in a higher resistance to corrosion
226 compared to the S275 steel. The surface of the S275 steel prior to deployment were
227 characterised by an irregular pattern (Figure 4A) as the coupons were used as provided by the
228 manufacturer (RS Components Ltd UK) and not polished again.

229

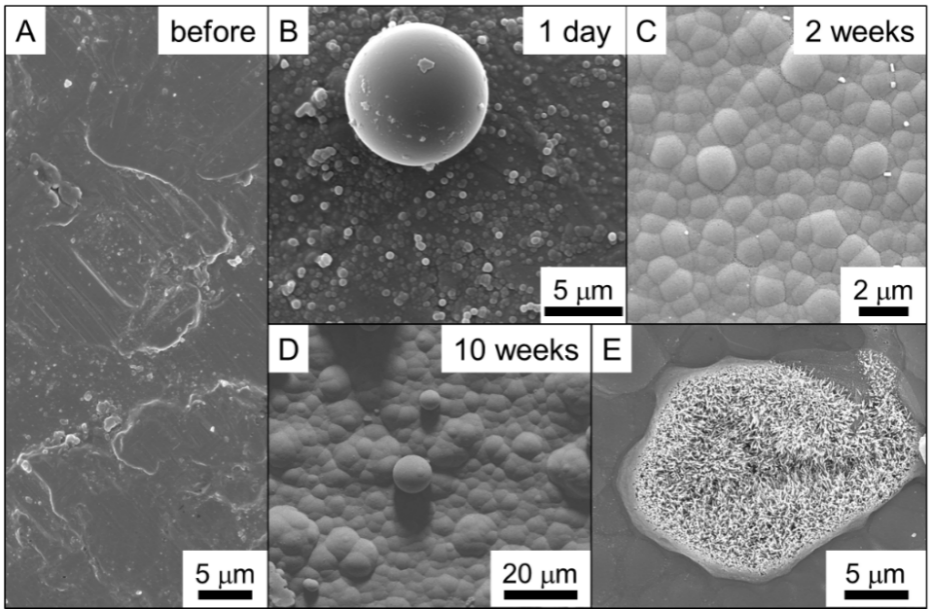

230

231 *Figure 4: FEG-SEM microphotographs of the carbon steel (S275) surface (A) before*
232 *deployment, (B) after 1 day, (C) after 2 weeks, (D) after 10 weeks and (E) close-up of Fe-*
233 *sulphides (= corrosion products, from van den Heuvel et al., 2016). All microphotographs*
234 *are from samples deployed at Location B.*

235

236 Despite using a high-grade adhesive to glue the coupons onto the stainless steel plates,
237 the following coupons became detached and were lost during the deployments:

238 - Opal: 6 week at Location A
239 - Volcanic glass: 6 week at Location A and B, 10 week at Location A

- Carbon steel: 1 week at Location A.

More plates were lost at Location A where the liquid is both hotter and faster flowing than at Location B. According to the manufacturer, the hot strength of the adhesive is identical for temperatures between 60 and 120°C. It is thus likely that the higher flow at Location A caused the plates to come off. In addition, for over half of the other opal and volcanic glass coupons, pieces broke off (a few μm^2 up to half of the coupon) and were lost during the deployment. Most commonly, the pieces were lost along the edge facing towards the flow. The partial loss of coupons prevented us from determining the amount of silica deposited based on the weight difference before and after deployment or the thickness of the silica layer as done by van den Heuvel et al. (2018) and therefore no silica precipitation rates could be quantified.

3.3 Description of silica precipitates post-deployment

All precipitates observed on the coupons consisted of impure amorphous silica (primarily containing Fe and Al) as confirmed by EDS (spot analyses) and XRD (bulk analyses). In addition, some Fe-rich phases formed on the carbon steel coupons (see below). The silica precipitates can be subdivided into two groups based on their morphologies: Individual and aggregated silica particles deposited onto all coupons, irrespective of the material. The silica particles were all spherical and ranged from <0.5 to around 20 μm in size with an average of ~3.5 μm at Location A and ~ 1.0 μm at Location B. They were preferentially deposited along topography, i.e. along the concoidal fractures in the opal (Figure 2E) as well as inside the vesicles in the volcanic glass (Figure 3E). On all coupons, the particles were also randomly distributed across the surface (Figure 2 B – D, 3 D and 4 B & D). For the 4 and 10 week deployments, fan-shaped 3D structures were observed along the edge of the scaling

plates/coupons oriented towards the flow (Figure 5A). They were formed by aggregation of individual silica particles from the liquid (Figure 5B & C), which were subsequently cemented by the deposition of dissolved silica, (Figure 5C). Over time, continued silica precipitation densified the structure, leading to a botryoidal morphology similar to the one described for the coupon surfaces below (Figure 5B I). Towards the edge, where particles were attached more recently, the structure is less cemented/more porous and the individual silica microspheres can still be identified (Figure 5B II). This relatively porous rim can be identified in Figure 5A due to its slightly lighter colour.

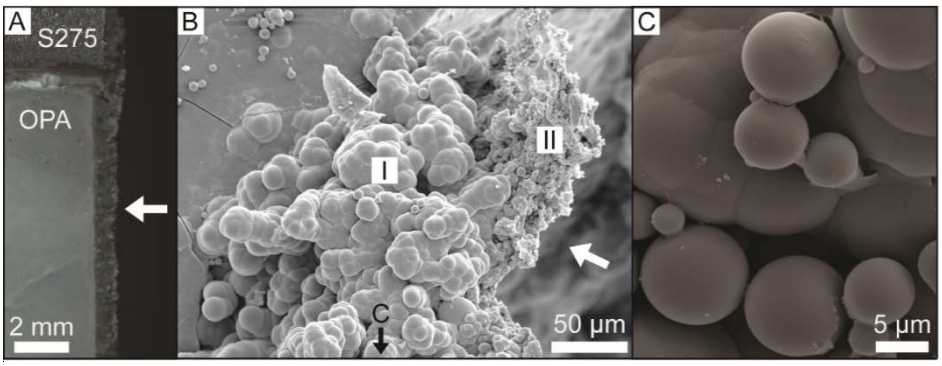

Figure 5: Photograph (A) and FEG-SEM microphotographs (B and C) of the 3D structures formed along the edge oriented towards the flow (flow direction indicated by arrows) by deposition of silica microspheres from the liquid and subsequent cementation by dissolved silica. Close to the plate, continued cementation by dissolved silica has densified the aggregates (I). The edge of the 3D structures consists of only weakly cemented aggregates of silica spheres (II), giving the outermost rim of the 3D structures a lighter colour. Photographs are from the 4-week sample deployed at Location A.

Silica also precipitated directly onto the surfaces, resulting in the formation of smooth "bumps" or half-spheres of silica. On the opal and volcanic glass surfaces, isolated half-

spheres formed during the short (i.e., up to 2 weeks) deployments (Figures 2B & C and 3B & C). They formed preferentially along superficial scratches (Figure 2E) or on the non-polished walls of the vesicles in the volcanic glass (Figure 3C). Their average size increased from 0.1 μm^2 to around 4.5 μm^2 at Location A and from 0.05 μm^2 to around 1 μm^2 at Location B (Figure 6) over the two weeks. Both coupon-types showed a similar size range and no systematic difference between the two materials could be observed. During the longer deployments (4 to 10 weeks), a continuous botryoidal layer formed (Figures 2D and 3D). The average size of individual half-spheres comprising the botryoidal layer increased from 11.5 μm^2 to over 90 μm^2 at Location A and from 2 μm^2 to around 11.5 μm^2 at Location B (Figure 6). Unfortunately, the volcanic glass coupons were lost for both, the 4 and 10 week deployment at Location A, preventing the comparison between opal and volcanic glass. However, at Location B the size range was near-identical for both materials which suggests that also during the longer deployments, there was no systematic difference between opal and volcanic glass.

In contrast to the opal and volcanic glass coupons, where a continuous layer only formed during the longer deployments, on the carbon steel such a botryoidal silica layer was already observed at the end of the 1-day deployment (Figure 4B). Interestingly, when comparing the size of the individual half-spheres for each deployment, they were similar to the individual half-spheres on opal and volcanic glass (Figure 6). Their sizes grew from 0.07 μm^2 after 1 day to over 90 μm^2 after 10 weeks at Location A and < 0.01 μm^2 to 15 μm^2 at Location B. In addition to the botryoidal silica layer, non-silica mineral phases were present on the carbon steel coupons (Figure 4E). These Fe- and S-containing phases co-evolved with the botryoidal silica layer from the moment the scaling plates were placed into the pipelines. They have previously been identified as corrosion products of carbon steel such

as mackinawite, gregite and their oxidation products hematite and goethite (van den Heuvel et al., 2016).

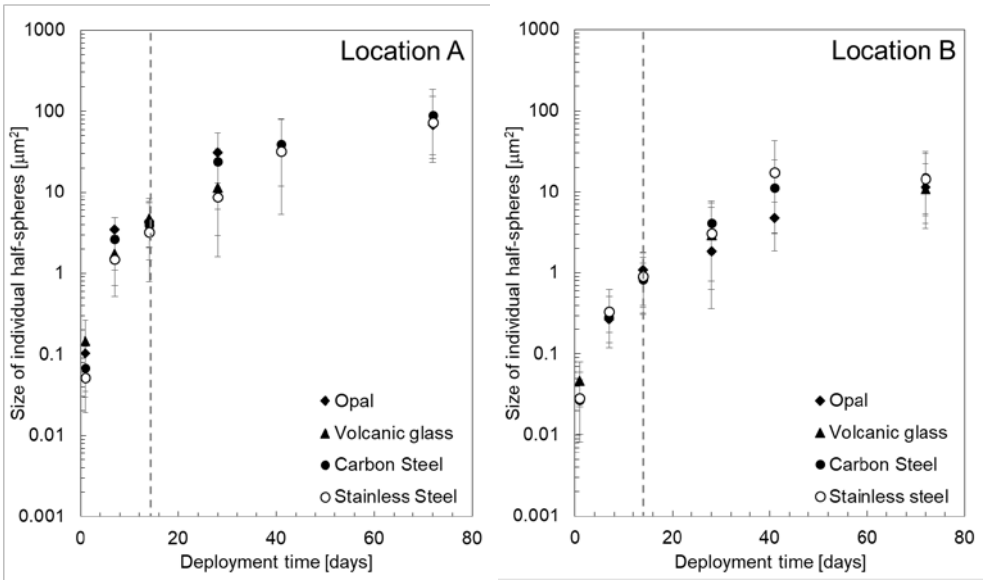

Figure 6: Evolution of the size of the individual half-spheres as a function of time (2 weeks indicated by dashed line) at Location A (left) and B (right) for all surfaces. The data points correspond to the average sizes while the bars indicate the size range from the smallest to the largest half-sphere measured. The stainless steel data are from van den Heuvel et al. (2018).

4. Discussion

4.1. Interactions between the separated water and the coupon materials

As the different surfaces were in contact with the separated water for up to 10 weeks, dissolution and/or alteration of the coupon materials were possible. In order to assess the likelihood of dissolution for the opal coupons, we compared the material to the silica gel used by Gunnarsson and Arnórsson (2000), which was used to determine the thermodynamic data, which in turn was used to calculate the SIs reported in Table 2. Potch opal consists of

irregularly packed submicrometre-sized spheres cemented together (Wollaert et al., 1990) while the silica gel consisted of porous silica spheres 63 to 200 μm in size. Purely based on the particle size, potch opal should be more soluble than the silica gel. However, the fact that the spheres in the opal are cemented and the ones in the silica particles porous suggests that potch opal is less soluble due to the substantially lower surface area. In addition, opal is not pure amorphous silica (~7 wt.% impurities, Table 1), while the silica gel was ultra-pure silica. Impurities lower the solubility of amorphous silica (Thórhallsson et al., 1975; Gallup, 1989; Gallup, 1998), supporting the idea that opal is less soluble than silica gel. As the fluid is supersaturated with respect to the amorphous silica gel (Table 2), it is expected to also be supersaturated with respect to opal. No dissolution of the opal coupons is thus expected.

Volcanic glass on the other hand is expected to react with the separated water as shown by a plethora of dissolution experiments in aqueous solutions. Using the dissolution rate of $1.5 \pm 0.51 \cdot 10^{-8}$ g_{glass} m^{-2} s^{-1} at ~80°C and pH 5.5-6 determined by Fiore et al. (1999) for rhyolitic obsidian dissolution, we calculated that the dissolution of our volcanic glass coupon (A = 2.6 cm^2, m = 1.1 g) is between 0.3 μg (1 day) and 24 μg (10 weeks), which corresponds to a dissolution of less than 0.002 wt.% of the total coupon. Using the rate by Fiore et al., we are likely overestimating dissolution at Location B (60 °C) while underestimating the dissolution at Location A (120 °C) as dissolution rates of volcanic glass increase with increasing temperature (Declercq et al., 2013). In addition, the used rate was determined at a lower pH than the pH inside the Hellisheiði pipelines (Table 2), suggesting that the calculated values overestimate dissolution as rates decrease strongly with increasing pH up to pH ~9 before increasing again at even higher pH values (Declercq et al., 2013). Despite these uncertainties regarding the dissolution rates, we can conclude that the amount of volcanic glass dissolved from the coupons is negligible. This is in line with the absence of rounded edges or precipitation of secondary phases (other than amorphous silica which is

precipitated due to supersaturation), both observations commonly made during dissolution experiments (Fiore et al., 1999; Declercq et al., 2013).

The S275 carbon steel is also highly reactive under in-situ conditions and Fe-sulphides, especially mackinawite (nominally FeS) is expected to form (Gao et al., 2018). Mackinawite was indeed observed on the S275 coupons, together with gregite (Fe_3S_4) as well as other, more oxidised iron minerals, which likely formed due to contact with atmospheric oxygen after removal of the plates from the pipelines (Figure 4E; van den Heuvel et al., 2016)

The limited dissolution/alteration of both, volcanic glass and carbon steel is not only related to the relatively low reactive surface area of the coupons but also to the formation of the silica layer, isolating the coupon surfaces from interaction with the separated water. The effect of an nm-scale amorphous silica layer on substrate dissolution rates has been investigated in the field of in-situ carbonation (Daval et al., 2009; Daval et al., 2011; Daval et al., 2013; Saldi et al., 2013) and silicate weathering rates (Hellmann et al., 2012; Ruiz-Agudo et al., 2012). Depending on the ratio of substrate dissolution rates (i.e. silicate hydrolysis) and precipitation rates of the silica layer, which in turn is determined by the mineral structure and composition of the substrate, impurities present in the silica layer (e.g. its Fe-content), temperature and interfacial liquid chemistry, a porous or dense silica layer develops. Non-porous silica layers have been shown to strongly reduce dissolution rates, e.g. of olivine (Daval et al., 2011; Saldi et al., 2013) and diopside (Daval et al., 2013) while porous layers are less effective (Daval et al., 2009). The internal structure of the silica layer formed during deployment inside the pipelines of the Hellisheiði power plant has been investigated previously (van den Heuvel et al., 2018). We could show that the layer is dense and with a thickness increasing from 0.3 to over 20 μm from 1 day to 10 weeks (at Location A). It is thus likely effective in passivating the surfaces against dissolution. For volcanic glass,

passivation only becomes effective for the longer deployments (4+ weeks) as for shorter periods no continuous silica layer has formed (Figure 3). The carbon steel coupons on the other hand are passivated much more rapidly as a continuous silica layer forms within a day, likely explaining the limited corrosion observed. However, as the corrosion products co-evolved with the botryoidal silica layer from the moment the scaling plates were placed into the pipelines, they may prevent complete passivation, explaining why some S275 coupons show signs of corrosion (see also van den Heuvel et al., 2016). Many of the coupons show cracks in the silica layer (e.g. Figure 3E). However, these cracks most likely formed post-deployment (during transport or drying) as no evidence for continued silica precipitation could be observed in any of these fractures. Thus, they do not challenge the passivation potential of amorphous silica scales.

4.2 Silica precipitation pathway

Two silica textures were observed on the scaling plates deployed inside the pipelines of the Hellisheiði power plant: silica particles deposited onto the coupons and a dense silica layer with a botryoidal surface. The results from our previous study showed that the two morphologies did not show the same evolution as a function of time and were controlled by different physicochemical conditions (hydrodynamics vs. liquid temperature and composition), indicating that they are the result of two different precipitation mechanisms, which take place independently of each other (van den Heuvel et al., 2018). As the scaling plates studied here were deployed concurrently to the stainless steel scaling plates studied previously (Figure 1) and both silica textures were observed on all samples, it was concluded that the silica precipitates described in Section 3.3 are also the result of precipitation via both, the homo- and heterogeneous pathway (Figure 7). As the separated water is only weakly supersaturated with respect to silica (Table 2), it is expected that precipitation via the

heterogeneous pathway is dominant (Iler, 1979; Weres et al., 1981). This is in line with the observation that on all surfaces, the botryoidal silica layer is more abundant than the silica particles deposited.

For the homogeneous pathway, the physicochemical conditions of the liquid alone control formation as homogeneous nucleation occurs in the absence of a surface (Figure 7). The conditions inside the pipelines at Hellisheiði are favourable for rapid nucleation and particle growth (i.e. elevated temperatures, high degree of monomeric silica and low ionic strength; Alexander et al., 1954; Weres et al., 1981; Bremere et al., 2000; Gunnarsson and Arnórsson, 2005; Icopini et al., 2005). Once the particles formed, their deposition was primarily controlled by surface morphology. The particles were preferentially deposited along the edges of the coupons and scaling plates as well as in the vesicles of the volcanic glass and the edges where pieces of opal broke off (Figure 2E). These edges, if oriented perpendicular to the flow direction, represent obstacles causing turbulent flow, which in turn favours particle deposition (e.g. Guha, 2008).

For the heterogeneous pathway, the physicochemical conditions of the liquid are also very important as they control nucleation and growth of the individual half-spheres. In this study, the physicochemical conditions were identical for the different coupons as they were glued onto the same stainless steel scaling plate (Figure 1). Thus, the difference observed between the opal, volcanic glass and S275 carbon steel has to be related to the different surface properties. Heterogeneous nucleation is controlled by properties such as composition and atomic structure of the substrate as well as surface roughness. Nucleation is enhanced if the surface is structurally and compositionally similar to the nucleating phase (De Yoreo and Vekilov, 2003; Fernandez-Martinez et al., 2012; Murray et al., 2012; Stockmann et al., 2014; Zolles et al., 2015). This suggests, that amorphous silica should nucleate most easily on opal as it is nearly pure amorphous silica (92.5% SiO_2, Table 1) and made up of individual silica

424 microspheres (Wollaert et al., 1990). The volcanic glass is also a siliceous and dominantly
425 amorphous material but with a higher concentration of non-silica constituents (69.5 wt. %
426 SiO_2, Table 1). It would therefore be expected to be less efficient at nucleating amorphous
427 silica than the opal. However, our data showed no difference between the formation of
428 amorphous silica on opal versus volcanic glass. On both coupons, isolated half-spheres
429 formed during the short deployments (Figures 2B & C and 3 B & C). Each of these half-
430 spheres represents a nucleation site. This shows that the nucleation sites are isolated and
431 randomly distributed across the surfaces. They are likely related to surface defects not visible
432 at the resolution studied here, where nucleation is energetically more favourable compared to
433 the rest of the surface (Benning and Waychunas, 2007). Nucleation also occurred along
434 visible defects such as superficial scratches on the opal (Figure 2 E) or the non-polished walls
435 of the vesicles in the volcanic glass (Figure 3E) which became covered in silica half-spheres
436 more rapidly. The similarities between opal and volcanic glass suggest that the chemical and
437 structural differences between the two materials are not substantial enough to affect the
438 precipitation behaviour at the conditions and scale studied here. This is in agreement with
439 previous studies, which showed that the development of a secondary silica layer during
440 silicate mineral dissolution was controlled by the relative rates of dissolution and
441 precipitation rather than substrate composition or structure (Daval et al., 2009; Daval et al.,
442 2011; Daval et al., 2013; Saldi et al., 2013). As dissolution was shown to be slow (volcanic
443 glass) or non-existent (opal), deposition of silica was controlled by the precipitation rate from
444 the separated water alone.

445 Throughout the deployments and independent of the coupon material, the half-spheres
446 were bigger at Location A compared to Location B (Figure 6). This can be explained by the
447 higher content of molybdate-reactive silica (primarily monomeric silica) as well as the higher
448 temperatures at Location A (Table 2). This is in agreement with a number of previous studies

449 who found that both of these factors enhances the formation of silica-silica bonds and thus
450 silica precipitation (Alexander et al., 1954; Kitahara, 1960; Bohlmann et al., 1976; Mroczek
451 and McDowell, 1988; Bremere et al., 2000; Gunnarsson and Arnórsson, 2003).

452

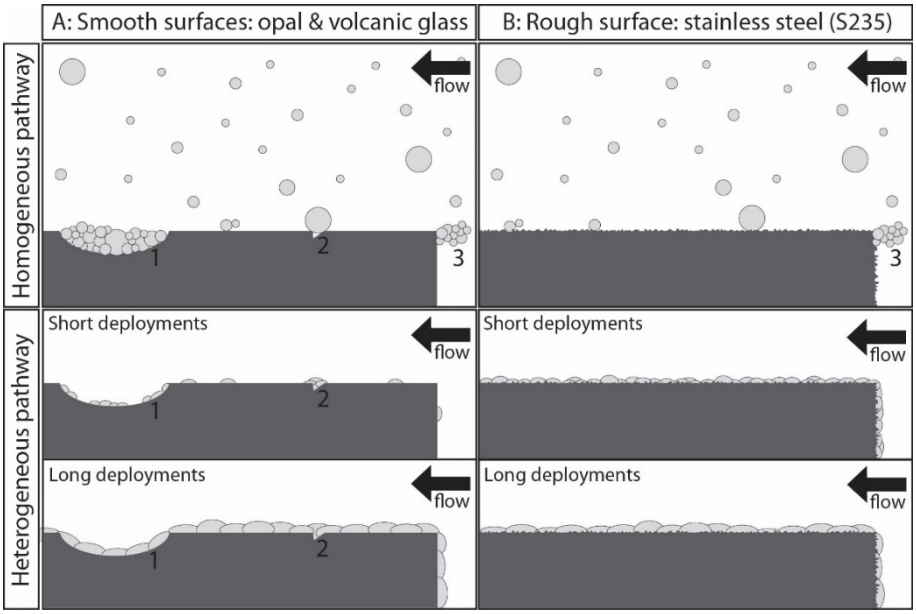

453

454 *Figure 7: Homogeneous and heterogeneous deposition of silica in the presence of (A) a*
455 *smooth surface and (B) a rough surface. On the rough surface, no preferential nucleation or*
456 *particle deposition was observed. On smooth surfaces on the other hand, vesicles (1) and*
457 *superficial scratches (2) acted as preferred nucleation and deposition sites. Homogeneously*
458 *nucleated silica particles were also deposited along the edge pointing towards the flow (3)*
459 *where they from 3D structures.*

460

461 The third type of coupon (S275 carbon steel) was expected to show a reduced
462 nucleation efficiency for amorphous silica due to its vastly different composition and
463 structure. Interestingly, our results showed the opposite: The carbon steel coupons were
464 completely covered in a botryoidal silica layer after just 1 day inside the pipelines (Figure

4B). This can be explained by the surface roughness of the steel coupons. Other than the opal and volcanic glass, the steel coupons showed a rough surface at the μm-scale (Figure 4A). This topography enhanced heterogeneous nucleation as it provided ample nucleation sites as well as a higher overall surface area (De Yoreo and Vekilov, 2003; Eastwood et al., 2008; Murray et al., 2012). This also explains the preferential nucleation of silica along scratches on the opal and the insides of vesicles on the volcanic glass (see above). Independent of the nucleation step, once formed, the individual half-spheres grew by addition of monomeric silica from the separated water via surface normal growth (Bohlmann et al., 1976; Mroczek and McDowell, 1988; Bremere et al., 2000; Jamtveit and Hammer, 2012; Noguera et al., 2015). Over time, this lead to the formation of a continuous botryoidal silica layer (Figures 2D, 3D and Figure 4B to D). While we observed a difference in the distribution of silica half-spheres (isolated nuclei vs. completely covered) between the different surfaces, their subsequent growth was comparable as shown by the similar sizes of the half-spheres within each deployment (Figure 6). This was to be expected because at this stage precipitation was controlled by silica-silica interactions alone and no longer affected by the coupon/scaling plate material. Thus, the precipitation rates determined by measuring the thickness of the botryoidal silica layer on the concurrently deployed stainless steel plates (van den Heuvel et al., 2018) can be applied to the samples studied here. This suggests that at Location A, precipitation decreased from around 900 mg m^{-2} day^{-1} after a week to around 630 mg m^{-2} day^{-1} after 10 weeks. For Location B, no comparable data was collected but the weight difference of the samples before and after deployment suggests slightly lower precipitation rates. These rates are comparable to silica precipitation rates measured at other geothermal power plants with similar physicochemical conditions, e.g. Ohaaki power station in New Zealand (Brown and McDowell, 1983) and the Sumikawa power plant in Japan (Okazaki et al., 2017).

The decrease in silica precipitation rates over time is mirrored in the growth rate of the half-spheres (Figure 6). In our previous study (van den Heuvel et al., 2018), we suggested that this decrease was because of the disappearance of half-sphere boundaries which act as preferential precipitation sites. However, if growth were indeed controlled by the number of such boundaries, we would expect to see a slower growth of half-spheres on the smooth surfaces where the silica mostly formed isolated half-spheres and thus the number of half-sphere boundaries is low. Based on the data presented here, this is not the case, suggesting that precipitation is equally likely across the whole surface of the half-spheres. Thus, the observed reduction of the half-sphere growth is likely only an apparent slowing down related to the ever-increasing surface area of the botryoidal silica layer while the deposition rate of silica from the fluid – solely depending on the physicochemical conditions of the fluid which were constant throughout the deployments (Table 2) – remained unchanged. This suggests that precipitation of silica, at least via the heterogeneous pathway, is controlled by interfacial processes and not diffusion limited.

4.3 Implications for the mitigation of silica scaling

Modification of surface properties to reduce or eliminate mineral scaling has been investigated for several years. Numerous groups have developed and tested anti-scaling coatings for Ca-carbonates and -sulphates such as alloy-containing epoxy-silicon resins, fluoropolymers or special nanopatterned surface textures (Malayeri et al., 2009; Wang et al., 2011; Wang et al., 2012; Oldani et al., 2015; Qian et al., 2017). Coatings specifically targeting silica scale formation were developed by Sugama et al. (2002). They developed and tested coatings composed of polyphenylenesulfide (PPS) and polytetrafluoro-ethylene (PTFE) specifically to combat silica scaling and tested it during an 11-month long field trial at Mammoth geothermal power station. Despite the surface coating, silica had precipitated.

514 However, the material deposited onto the relatively smooth surface was less adherent and
515 easier to remove by hydroblasting, substantially reducing the maintenance effort. The
516 observed silica scaling is in line with our findings, showing that, while surface properties
517 affect the onset of silica scaling, they cannot prevent precipitation from happening.

518 In addition, the scaling plate studies at the Hellisheiði power plant show that silica
519 does not only precipitate as a dense layer but also forms particles, which are deposited onto
520 available surfaces. Our results showed that the particles are deposited primarily along edges
521 (of the scaling plates/coupons or fractures), where liquid flow becomes turbulent and
522 particles are more likely to be deposited (e.g. Guha, 2008). The complex geometry of the
523 flow path within a geothermal power plant (e.g. bends, reduction in pipe diameter, valves,
524 and inlets) results in a large number of obstacles where flow becomes turbulent and the
525 deposition of homogeneously nucleated silica particles is thus likely enhanced. These
526 preferred deposition sites cannot be eliminated by anti-scaling coatings.

527 This suggests that overall, anti-scaling coatings are not an effective means to prevent
528 silica scaling from occurring as they only affect one of the two precipitation pathways. In
529 order to successfully mitigate silica scaling, strategies targeting the homogeneous pathway
530 too, ideally by inhibiting silica polymerisation, need to be developed.

531

532 **5. Summary**

533 The results of our scaling plate study at Hellisheiði showed that silica can precipitate via a
534 homogeneous and a heterogeneous pathway inside geothermal pipelines. While the
535 homogeneous pathway is independent of the characteristics of available surfaces, the
536 heterogeneous pathway is controlled by their properties. In this study, we investigated
537 materials which are present in a geothermal system (opal = previously formed silica scales,

538 volcanic glass = reservoir rocks, carbon steel = pipelines) for their ability to enhance silica
539 precipitation via the heterogeneous pathway. Based on structural and chemical similarities,
540 opal should have been the most effective surface at nucleating silica, followed by volcanic
541 glass while precipitation onto carbon steel should have been limited. In reality, nucleation on
542 carbon steel was fastest due to its rough surface. This suggests that, at least for the samples
543 studied here, similarities (both, structurally and chemically) between the substrate and the
544 precipitating silica was less important than surface roughness in enhancing scaling. In order
545 to understand the interplay between surface structure/composition and roughness in more
546 detail, more surfaces would need to be investigated. However, as surface properties only
547 affected the initial stages of the heterogeneous pathway, such an extended study is not crucial
548 for the development of better mitigation strategies against silica scaling.

549

550 **Acknowledgments**

551 This research was made possible by a Marie Curie grant from the European Commission in
552 the framework of the MINSC ITN (Initial Training Research network), Project number
553 290040, the 2014 PhD Student Grant by the International Geothermal Association (IGA)
554 awarded to DBH and a UK Natural Environment Research Council grant (NE/J008745/1)
555 awarded to LGB. We thank GT Opals in Coober Peedy for providing the non-precious opal
556 samples and Tony Windross, Stephen Burgess and Hari Williams for preparation of all plates
557 and coupons. We are grateful to Gisela Weibel at the University of Bern for XRF analyses.
558 We would like to thank the local staff at Hellisheiði, especially Halldór Bergmann, for help
559 with sampling and are grateful to the laboratory staff at Reykjavik energy and Stephen Reid,
560 Fiona Keay and Richard Walshaw at the University of Leeds for liquid analyses as well as for
561 support with SEM analyses. We would also like to thank Ch. Bromley (Editor) and H.

562 Ármannsson (Associate Editor) of *Geothermics* and two anonymous reviewers for their
563 contributions to this paper.

564 References
565
566 Alexander, G.B., Heston, W. and Iler, R.K. (1954) The solubility of amorphous silica in
567 water. The Journal of Physical Chemistry 58, 453-455.

568 Alfredsson, H.A., Oelkers, E.H., Hardarsson, B.S., Franzson, H., Gunnlaugsson, E. and
569 Gislason, S.R. (2013) The geology and water chemistry of the Hellisheiði, SW-Iceland
570 carbon storage site. International Journal of Greenhouse Gas Control 12, 399-418.

571 Arnórsson, S., Bjarnason, J.Ö., Giroud, N., Gunnarsson, I. and Stefánsson, A. (2006)
572 Sampling and analysis of geothermal fluids. Geofluids 6, 203-216.

573 Benning, L.G. and Waychunas, G.A. (2007) Nucleation, growth, and aggregation of mineral
574 phases: Mechanisms and kinetic controls, Kinetics of Water-Rock Interaction. Springer, pp.
575 259-333.

576 Bohlmann, E., Shor, A. and Berlinski, P. (1976) Precipitation and scaling in dynamic
577 geothermal systems. NASA STI/Recon Technical Report N 77.

578 Bremere, I., Kennedy, M., Mhyio, S., Jaljuli, A., Witkamp, G.-J. and Schippers, J. (2000)
579 Prevention of silica scale in membrane systems: removal of monomer and polymer silica.
580 Desalination 132, 89-100.

581 Brown, K. and McDowell, G. (1983) pH control of silica scaling, Proceedings of the 5th New
582 Zealand Geothermal Workshop, New Zealand, pp. 157-161.

583 Campbell, J.M., Meldrum, F.C. and Christenson, H.K. (2013) Characterization of preferred
584 crystal nucleation sites on mica surfaces. Crystal Growth & Design 13, 1915-1925.

585 Carroll, S., Mroczek, E., Alai, M. and Ebert, M. (1998) Amorphous silica precipitation (60 to
586 120 C): Comparison of laboratory and field rates. Geochimica et Cosmochimica Acta 62,
587 1379-1396.

588 Crerar, D.A., Axtmann, E.V. and Axtmann, R.C. (1981) Growth and ripening of silica
589 polymers in aqueous solutions. Geochimica et Cosmochimica Acta 45, 1259-1266.

590 Daval, D., Hellmann, R., Saldi, G.D., Wirth, R. and Knauss, K.G. (2013) Linking nm-scale
591 measurements of the anisotropy of silicate surface reactivity to macroscopic dissolution rate
592 laws: New insights based on diopside. Geochimica et Cosmochimica Acta 107, 121-134.

593 Daval, D., Martinez, I., Corvisier, J., Findling, N., Goffé, B. and Guyot, F. (2009)
594 Carbonation of Ca-bearing silicates, the case of wollastonite: Experimental investigations and
595 kinetic modeling. Chemical Geology 265, 63-78.

596 Daval, D., Sissmann, O., Menguy, N., Saldi, G.D., Guyot, F., Martinez, I., Corvisier, J.,
597 Garcia, B., Machouk, I. and Knauss, K.G. (2011) Influence of amorphous silica layer

598 formation on the dissolution rate of olivine at 90 C and elevated pCO2. Chemical Geology
599 284, 193-209.

600 De Yoreo, J.J. and Vekilov, P.G. (2003) Principles of crystal nucleation and growth. Reviews
601 in mineralogy and geochemistry 54, 57-93.

602 Declercq, J., Diedrich, T., Perrot, M., Gislason, S.R. and Oelkers, E.H. (2013) Experimental
603 determination of rhyolitic glass dissolution rates at 40–200 C and 2<pH<10.1. Geochimica et
604 Cosmochimica Acta 100, 251-263.

605 Dixit, C., Bernard, M.-L., Sanjuan, B., André, L. and Gaspard, S. (2016) Experimental study
606 on the kinetics of silica polymerization during cooling of the Bouillante geothermal fluid
607 (Guadeloupe, French West Indies). Chemical Geology 442, 97-112.

608 Eastwood, M.L., Cremel, S., Gehrke, C., Girard, E. and Bertram, A.K. (2008) Ice nucleation
609 on mineral dust particles: Onset conditions, nucleation rates and contact angles. Journal of
610 Geophysical Research: Atmospheres 113.

611 Fernandez-Martinez, A., Hu, Y., Lee, B., Jun, Y.-S. and Waychunas, G.A. (2012) In situ
612 determination of interfacial energies between heterogeneously nucleated CaCO3 and quartz
613 substrates: thermodynamics of CO2 mineral trapping. Environmental science & technology
614 47, 102-109.

615 Fiore, S., Huertas, F.J., Tazaki, K., Huertas, F. and Linares, J. (1999) A low temperature
616 experimental alteration of a rhyolitic obsidian. European Journal of Mineralogy, 455-470.

617 Fleming, B. and Crerar, D. (1982) Silicic acid ionization and calculation of silica solubility at
618 elevated temperature and pH application to geothermal fluid processing and reinjection.
619 Geothermics 11, 15-29.

620 Gallup, D. (1989) Iron silicate scale formation and inhibition at the Salton Sea geothermal
621 field. Geothermics 18, 97-103.

622 Gallup, D.L. (1997) Aluminum silicate scale formation and inhibition: scale characterization
623 and laboratory experiments. Geothermics 26, 483-499.

624 Gallup, D.L. (1998) Aluminum silicate scale formation and inhibition (2): scale solubilities
625 and laboratory and field inhibition tests. Geothermics 27, 485-501.

626 Gao, S., Brown, B., Young, D. and Singer, M. (2018) Formation of iron oxide and iron
627 sulfide at high temperature and their effects on corrosion. Corrosion Science 135, 167-176.

628 Goto, K. (1956) Precipitation of silica in the presence of aluminum. Bulletin of the Chemical
629 Society of Japan 29, 740-741.

630 Gudmundsson, J.S. and Bott, T.R. (1979) Deposition of silica from geothermal waters on
631 heat transfer surfaces. Desalination 28, 125-145.

632 Guha, A. (2008) Transport and deposition of particles in turbulent and laminar flow. Annu.
633 Rev. Fluid Mech. 40, 311-341.

634 Gunnarsson, I. and Arnórsson, S. (2000) Amorphous silica solubility and the thermodynamic
635 properties of H4SiO 4 in the range of 0 to 350 C at Psat. Geochimica et Cosmochimica Acta
636 64, 2295-2307.

637 Gunnarsson, I. and Arnórsson, S. (2003) Silica scaling: The main obstacle in efficient use of
638 high-temperature geothermal fluids, Proceedings International Geothermal Conference,
639 Reykjavik, pp. 30-36.

640 Gunnarsson, I. and Arnórsson, S. (2005) Impact of silica scaling on the efficiency of heat
641 extraction from high-temperature geothermal fluids. Geothermics 34, 320-329.

642 Gunnarsson, I., Ívarsson, G., Sigfússon, B., Thrastarson, E.Ö. and Gíslason, G. (2010)
643 Reducing silica deposition potential in waste waters from Nesjavellir and Hellisheiði Power
644 Plants, Iceland, Proceedings World Geothermal Congress, Bali.

645 Harrar, J., Locke, F., Otto Jr, C., Lorensen, L., Monaco, S. and Frey, W. (1982) Field tests of
646 organic additives for scale control at the Salton Sea geothermal field. Society of Petroleum
647 Engineers Journal 22, 17-27.

648 Hellmann, R., Wirth, R., Daval, D., Barnes, J.-P., Penisson, J.-M., Tisserand, D., Epicier, T.,
649 Florin, B. and Hervig, R.L. (2012) Unifying natural and laboratory chemical weathering with
650 interfacial dissolution–reprecipitation: a study based on the nanometer-scale chemistry of
651 fluid–silicate interfaces. Chemical Geology 294, 203-216.

652 Icopini, G.A., Brantley, S.L. and Heaney, P.J. (2005) Kinetics of silica oligomerization and
653 nanocolloid formation as a function of pH and ionic strength at 25 C. Geochimica et
654 Cosmochimica Acta 69, 293-303.

655 Iler, R.K. (1979) The chemistry of silica: solubility, polymerization, colloid and surface pro
656 perties, and biochemistry. Wiley, London.

657 Jamtveit, B. and Hammer, Ø. (2012) Sculpting of rocks by reactive fluids. Geochemical
658 Perspectives 1, 341-342.

659 Järn, M., Areva, S., Pore, V., Peltonen, J. and Linden, M. (2006) Topography and Surface
660 Energy Dependent Calcium Phosphate Formation on Sol− Gel Derived TiO2 Coatings.
661 Langmuir 22, 8209-8213.

662 Kitahara, S. (1960) The polymerization of silicic acid obtained by the hydrothermal treatment
663 of quartz and the solubility of amorphous silica.

Malayeri, M., Al-Janabi, A. and Müller-Steinhagen, H. (2009) Application of nano-modified surfaces for fouling mitigation. International journal of energy research 33, 1101-1113.

Meier, D., Gunnlaugsson, E., Gunnarsson, I., Jamtveit, B., Peacock, C. and Benning, L. (2014) Microstructural and chemical variation in silica-rich precipitates at the Hellisheiði geothermal power plant. Mineralogical Magazine 78, 1381-1389.

Mroczek, E., Graham, D., Siega, C. and Bacon, L. (2017) Silica scaling in cooled silica saturated geothermal water: Comparison between Wairakei and Ohaaki geothermal fields, New Zealand. Geothermics 69, 145-152.

Mroczek, E. and McDowell, G. (1988) Silica scaling field experiments. Proceedings 10th New Zealand Geothermal Workshop, 281-284.

Murray, B., O'Sullivan, D., Atkinson, J. and Webb, M. (2012) Ice nucleation by particles immersed in supercooled cloud droplets. Chemical Society Reviews 41, 6519-6554.

Noguera, C., Fritz, B. and Clément, A. (2015) Precipitation mechanism of amorphous silica nanoparticles: A simulation approach. Journal of colloid and interface science 448, 553-563.

Oldani, V., Del Negro, R., Bianchi, C.L., Suriano, R., Turri, S., Pirola, C. and Sacchi, B. (2015) Surface properties and anti-fouling assessment of coatings obtained from perfluoropolyethers and ceramic oxides nanopowders deposited on stainless steel. Journal of Fluorine Chemistry 180, 7-14.

Padilla, S.R.M., Barnett, P., Castro, M., Guerra, E. and Henríquez, J.L. (2005) Silica polymerization and deposition trials at the Berlin geothermal Field, El Salvador, World Geothermal Congress, Antalya, Turkey, pp. 1-4.

Page, A.J. and Sear, R.P. (2009) Crystallization controlled by the geometry of a surface. Journal of the American Chemical Society 131, 17550-17551.

Parkhurst, D.L. and Appelo, C. (2013) Description of input and examples for PHREEQC version 3: a computer program for speciation, batch-reaction, one-dimensional transport, and inverse geochemical calculations. US Geological Survey.

Putnis, A. (2009) Mineral replacement reactions. Reviews in mineralogy and geochemistry 70, 87-124.

Qi, Y., Klausner, J.F. and Mei, R. (2004) Role of surface structure in heterogeneous nucleation. International Journal of Heat and Mass Transfer 47, 3097-3107.

Qian, H., Zhu, Y., Wang, H., Song, H., Wang, C., Liu, Z. and Li, H. (2017) Preparation and antiscaling performance of superhydrophobic poly (phenylene sulfide)/polytetrafluoroethylene composite coating. Industrial & Engineering Chemistry Research 56, 12663-12671.

Rothbaum, H., Anderton, B., Harrison, R., Rohde, A. and Slatter, A. (1979) Effect of silica polymerisation and pH on geothermal scaling. Geothermics 8, 1-20.

Ruiz-Agudo, E., Putnis, C.V., Rodriguez-Navarro, C. and Putnis, A. (2012) Mechanism of leached layer formation during chemical weathering of silicate minerals. Geology 40, 947-950.

Saldi, G.D., Daval, D., Morvan, G. and Knauss, K.G. (2013) The role of Fe and redox conditions in olivine carbonation rates: An experimental study of the rate limiting reactions at 90 and 150 C in open and closed systems. Geochimica et Cosmochimica Acta 118, 157-183.

Stockmann, G.J., Wolff-Boenisch, D., Bovet, N., Gislason, S.R. and Oelkers, E.H. (2014) The role of silicate surfaces on calcite precipitation kinetics. Geochimica et Cosmochimica Acta 135, 231-250.

Sugama, T., Elling, D. and Gawlik, K. (2002) Poly (phenylenesulfide)-based coatings for carbon steel heat exchanger tubes in geothermal environments. Journal of materials science 37, 4871-4880.

Thórhallsson, S., Ragnars, K., Arnórsson, S. and Kristmannsdóttir, H. (1975) Rapid scaling of silica in two district heating systems, 2nd United Nations Symposium on the Development and Use of Geothermal Resources, San Fransico, pp. 1445-1449.

Tobler, D.J. and Benning, L.G. (2013) In situ and time resolved nucleation and growth of silica nanoparticles forming under simulated geothermal conditions. Geochimica et Cosmochimica Acta 114, 156-168.

Tobler, D.J., Shaw, S. and Benning, L.G. (2009) Quantification of initial steps of nucleation and growth of silica nanoparticles: An *in-situ* SAXS and DLS study. Geochimica et Cosmochimica Acta 73, 5377-5393.

van den Heuvel, D.B., Gunnlaugsson, E. and Benning, L.G. (2016) Passivation of metal surfaces against corrosion by silica scaling, Proceedings Workshop on Geothermal Reservoir Engineering Stanford.

van den Heuvel, D.B., Gunnlaugsson, E., Gunnarsson, I., Stawski, T.M., Peacock, C.L. and Benning, L.G. (2018) Understanding amorphous silica scaling under well-constrained conditions inside geothermal pipelines. Geothermics 76, 231-241.

Wang, G., Zhu, L., Liu, H. and Li, W. (2011) Zinc-graphite composite coating for anti-fouling application. Materials Letters 65, 3095-3097.

Wang, G., Zhu, L., Liu, H. and Li, W. (2012) Galvanic corrosion of Ni–Cu–Al composite coating and its anti-fouling property for metal pipeline in simulated geothermal water. Surface and Coatings Technology 206, 3728-3732.

732 Weres, O., Yee, A. and Tsao, L. (1981) Kinetics of silica polymerization. Journal of Colloid
733 and Interface Science 84, 379-402.

734 Wolff-Boenisch, D., Gislason, S.R., Oelkers, E.H. and Putnis, C.V. (2004) The dissolution
735 rates of natural glasses as a function of their composition at pH 4 and 10.6, and temperatures
736 from 25 to 74 C. Geochimica et Cosmochimica Acta 68, 4843-4858.

737 Wollaert, E., Vochten, R. and Van Landuyt, J. (1990) Characterisation of Gem Opal and
738 Inferior Opal Qualities by Means of Electronmicroscopy. E. Schweizerbartsche
739 Verlagsbuchhandlung.

740 Yokoyama, T., Sato, Y., Maeda, Y., Tarutani, T. and Itoi, R. (1993) Siliceous deposits
741 formed from geothermal water I. The major constituents and the existing states of iron and
742 aluminium. Geochemical Journal 27, 375-384.

743 Zolles, T., Burkart, J., Häusler, T., Pummer, B., Hitzenberger, R. and Grothe, H. (2015)
744 Identification of ice nucleation active sites on feldspar dust particles. The Journal of Physical
745 Chemistry A 119, 2692-2700.

746

747